Molecular Beam Epitaxy of Highly Crystalline MoSe₂ on Hexagonal Boron Nitride

Sock Mui Poh,[†,‡,&] Xiaoxu Zhao,[†,‡,&] Sherman Jun Rong Tan,[†,‡] Deyi Fu,[‡,§] Wenwen Fei,[∥] Leiqiang Chu,[‡,§] Dan Jiadong,[†,⊥] Wu Zhou,[#] Stephen J. Pennycook,[†,§,⊥] Antonio H. Castro Neto,[§,⊗] and Kian Ping Loh*[,‡,§,▽]

†NUS Graduate School for Integrative Sciences and Engineering, Centre for Life Sciences #05-01, 28 Medical Drive, 117456, Singapore

‡Department of Chemistry, National University of Singapore, Science Drive 3, 117543, Singapore

§Centre for Advanced 2D Materials and Graphene Research Centre, National University of Singapore, 117546, Singapore

∥State Key Laboratory of Mechanics and Control of Mechanical Structures, Key Laboratory for Intelligent Nanomaterials and Devices of the MOE, Institute of Nanoscience, Nanjing University of Aeronautics and Astronautics, Nanjing 210016, China

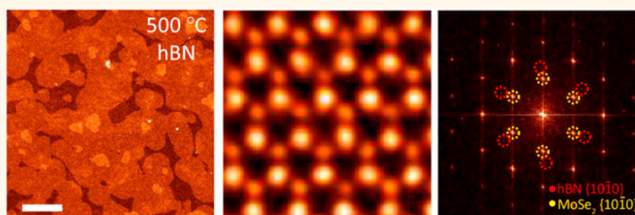⊥Department of Materials Science and Engineering, National University of Singapore, 117575, Singapore

#School of Physical Sciences and CAS Centre for Excellence in Topological Quantum Computation, University of Chinese Academy of Sciences, Beijing, 100049, China

⊗Department of Physics, National University of Singapore, 3 Science Drive 2, 117542, Singapore

▽SinBeRISE CREATE and C4T CREATE, National Research Foundation, CREATE Tower, 1 Create Way, 138602, Singapore

Ⓢ Supporting Information

ABSTRACT: Molybdenum diselenide (MoSe₂) is a promising two-dimensional material for next-generation electronics and optoelectronics. However, its application has been hindered by a lack of large-scale synthesis. Although chemical vapor deposition (CVD) using laboratory furnaces has been applied to grow two-dimensional (2D) MoSe₂ cystals, no continuous film over macroscopically large area has been produced due to the lack of uniform control in these systems. Here, we investigate the molecular beam epitaxy (MBE) of 2D MoSe₂ on hexagonal boron nitride (hBN) substrate, where highly crystalline MoSe₂ film can be grown with electron mobility ∼15 cm²/(V s). Scanning transmission electron microscopy (STEM) shows that MoSe₂ grains grown at an optimum temperature of 500 °C are highly oriented and coalesced to form continuous film with predominantly mirror twin boundaries. Our work suggests that van der Waals epitaxy of 2D materials is tolerant of lattice mismatch but is facilitated by substrates with similar symmetry.

KEYWORDS: two-dimensional transition metal dichalcogenides, MoSe₂, molecular beam epitaxy, field-effect transistor, mobility, grain boundaries

Transition-metal dichalcogenides (TMDCs) are of great interest as they exhibit quantum properties in the two-dimensional limit,[1−6] with promising prospects for next-generation electronics,[7−10] optoelectronics,[11−14] and catalytic applications.[15−17] 2D MoS₂ has been extensively studied owing to it being a stable semiconductor that can complement zero-bandgap graphene.[18] Similar to MoS₂, MoSe₂ exhibits interesting 2D properties such as indirect–direct bandgap transition,[19] strong photoluminescence,[20] degenerate valleys,[2] and catalytic properties.[21] In addition, MoSe₂ possesses several advantages compared to MoS₂: stronger spin–orbit coupling which can be utilized in spintronic applications,[19] highly stable tunable ambipolar

charge excitons,[22] narrower bandgap for solar cell applications,[20] thermally accessible bandgap transition,[23] higher optical absorbance[24] and faster photoresponse.[25] Yet, the growth of MoSe₂ has received much less attention than MoS₂[26] and there is still a lack of reliable technique for its large-scale growth.

Chemical vapor deposition (CVD) is the most common growth technique for 2D TMDCs. Compared to MoS₂, the growth of 2D MoSe₂ is more difficult as it uses solid Se, which

is less reactive and requires additional H_2 gas as reductant.[25,27−33] Common to all tube furnace-based CVD processes, the as-grown film is highly inhomogeneous across macroscopic length scales[30,31,33] due to the nonuniform temperature gradient and precursor vapor concentrations along the furnace tube. In contrast, MBE offers significant advantages for the growth of highly uniform, wafer-scale 2D TMDC film because the substrate temperature is decoupled from the evaporation temperature of the growth precursors, thus affording precise control in the growth rate of the film. Wafer-scale growth of 2D MoSe₂ which shows good electrical quality has not been achieved to date. Reported electron mobilities of field-effect transistors (FETs) fabricated from the synthesized 2D $MoSe_2$ ranges from 0.02 to 95 cm²/(V s)[25,27,30,32−34] and for thicker samples of >10 nm, the mobilities range from 100 to 160 cm²/(V s).[35,36] However, the growth of such thick samples is of less significance since the desired two-dimensional properties only exist when $MoSe_2$ is a few layers thick. A comparison of the previous works on vapor-phase growth of $MoSe_2$ is summarized in Table I.

Table I. Consolidation of Reported MoSe₂ Vapor-Phase Growth

year	method	substrate	device performance/remarks	ref
2017	MBE	hBN	15 cm²/(V s)	this work
2017	MBE	GaAs(111)	electrons: 0.05 cm²/(V s), holes: 0.28 cm²/(V s)	37
2017	MBE	sapphire	insulating	38
2016	MBE	sapphire	insulating	39
2017	CVD	Glass	5−95 cm²/(V s), inhomogeneous	34
2016	CVD	SiO₂/Si	42 cm²/(V s), inhomogeneous	33
2015	CVD	Mo/Si	121 cm²/(V s), thick growth	36
2015	CVD	SiO₂/Si	10 cm²/(V s), inhomogeneous, micron-scale	32
2014	CVD	SiO₂/Si	50 cm²/(V s), inhomogeneous, micron-scale	30
2014	CVD	Sapphire	15−23 cm²/(V s), inhomogeneous; micron-scale	25
2014	CVD	Parylene-C/ SiO₂/Si	100−160 cm²/(V s), thick growth	35
2014	CVD	SiO₂/Si	electrons: 0.02 cm²/(V s), holes: 0.01 cm²/(V s)	27
2014	CVD	SiO₂/Si, Mica, Si	device no mobility	31
2014	CVD	SiO₂/Si, Sapphire	no device	29
2014	CVD	SiO₂/Si	no device	28

Molecular beam epitaxy (MBE) provides high precision in the control of growth temperature and precursor flux, as well as the use of a contaminant-free environment. The MBE of $MoSe_2$ has been demonstrated to produce high quality growth on metallic substrates, which enabled fundamental studies of 2D-TMDC system.[19,40,41] However, the electrical performance of MBE grown samples are rarely reported.[19,37,40−46] Thus far, MBE-grown $MoSe_2$ on GaAs(111) substrate exhibits mobility values of <1 cm²/(V s),[47] and on sapphire substrates, the grown films are insulating[38,39] (Table I). This indicates that the choice of substrate can drastically affect the electrical performance of MBE-grown film.

Herein, we demonstrate the MBE growth of 1−2 layers $MoSe_2$ on van der Waals (vdW) substrate hBN, with an average field-effect electron mobility of ∼14.7 ± 0.8 cm²/(V s).

Although the lattice mismatch can be as high as 24% between $MoSe_2$ and hBN, the ultraflat and dangling-bond free nature of hBN appears to be a more important factor than its lattice matching condition for the vdW epitaxy of 2D materials. Importantly, FET devices can be directly fabricated on the as-grown film using hBN as the dielectric layer, the latter is known to reduce Coulomb scattering and greatly improve the electrical performance.[48] High-resolution transmission electron microscopy (HRTEM) is applied to study the defects and grain boundaries in $MoSe_2$ films grown at different temperatures in order to obtain insights on how high quality crystalline film is grown.

RESULTS AND DISCUSSION

We investigated the change in growth morphology of films grown on hBN at 250 and 500 °C as a function of time using atomic force microscopy (AFM), as shown in Figure 1a−c and Figure 1d−f. Their respective growth rates are found to be ∼0.6 and ∼1.3 ML/h. The Se flux was always maintained in large excess to Mo at a ratio of ∼20:1 (refer to the Methods). The height of each grown layer was measured to be ∼0.7 nm, which corresponds to the height of a layer of MoSe₂[7] (inset of Figure 1e). Striking differences were observed for the growth morphology at these two temperatures, in which a higher temperature resulted in a much larger domain size and lower domain density (Figure 1e vs b). These can be rationalized on the basis of a higher diffusion rate of surface adatoms and Ostwald ripening of the grains at higher growth temperatures.[49,50] When the substrate temperature is too low, adatoms cannot overcome diffusion barriers and a high nucleation density results.[52] Importantly, a high growth temperature allows sufficient mobility of the adatoms such that the domains can be aligned with the substrate crystallographic orientation, leading to their seamless merging to form a continuous film (Figure 1f) in the case of perfectly aligned grains, or forming well-stitched, low-energy mirror twin grain boundaries (MTBs) for grains that are rotated 60° with respect to each other.[51] (see section on STEM). Growth at a lower temperature on the other hand, tends to form gaps between the grains (Figure 1c), which eventually merged to form odd numbered 5|7-fold rings of dislocation cores (see TEM discussion). However, 500 °C is identified as the optimal temperature for film growth of $MoSe_2$ because at higher temperatures the much higher desorption rate of Se adatoms drive the growth mode to one-dimensional growth and nanoribbons were produced instead, which had been reported in our earlier study.[52]

The evolution in growth morphology of the crystals with temperature agrees well with the diffusion-limited aggregation (DLA) growth theory,[53] which predicts a fractal growth mode when surface diffusion is rate-limiting. A low temperature growth produced faceted domains (Figure 1a,b), whereas compact and round-shaped domains (Figure 1d and e) were obtained at high temperature growth. At sufficiently high temperature, the adatoms can overcome diffusion barrier and flow along the edges to form energetically favored compact shape.[50] The effect of temperature on the domain shape was further verified by performing growth studies at increasing temperatures to observe the morphological evolution (Figure S1), in which the edges of facets become increasingly rounded at higher growth temperatures. As the diffusion rate of Mo adatoms is much lower than Se adatoms,[54] diffusion-limited growth is also observed when the Se flux is reduced
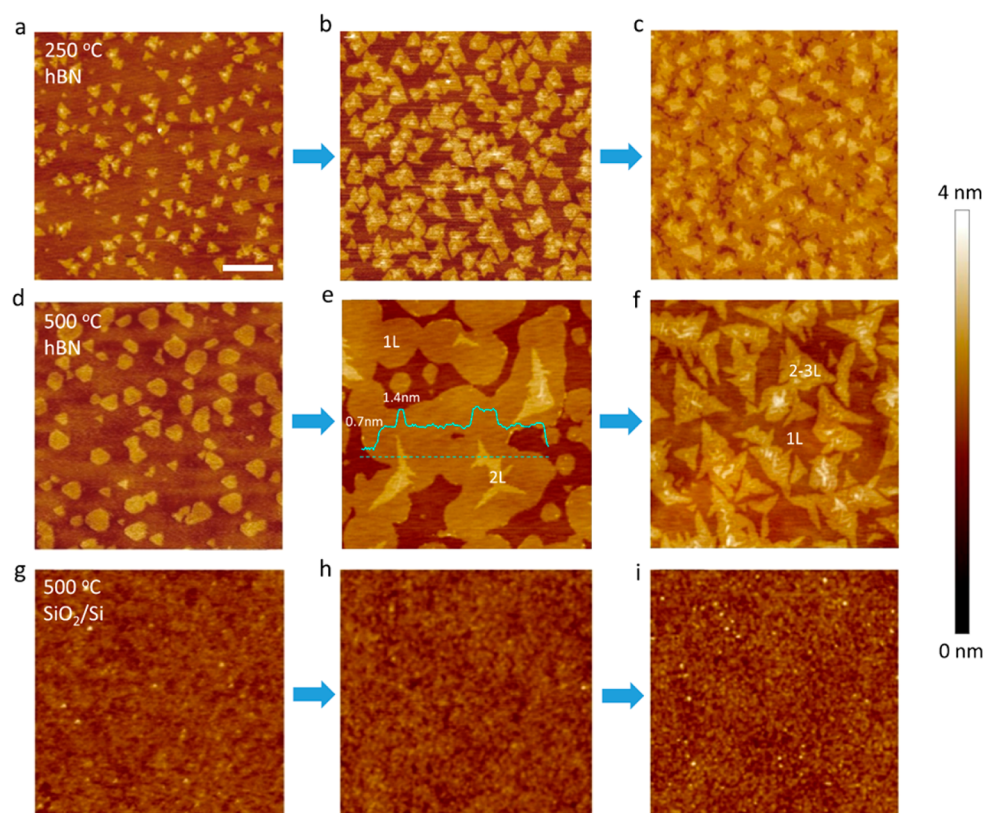
Figure 1. AFM topograph of growth progress of MBE-grown MoSe₂ on hBN at substrate temperature of 250 °C (a−c) and 500 °C (d−f), and on SiO₂/Si at 500 °C (g−i). Arrows indicate increasing growth duration. All of the images are of the same scale bar: 200 nm.
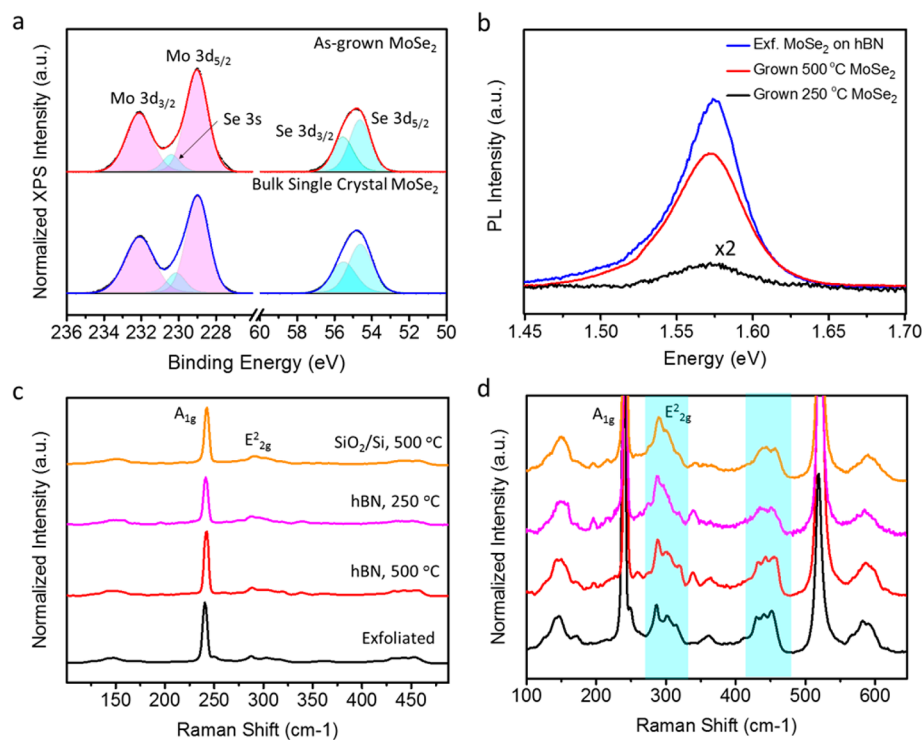

Figure 2. Spectroscopic characterization. (a) XPS spectra of MBE-grown MoSe₂ and bulk single crystal for the Mo core level peaks and Se core level peaks. (b) PL of MBE-grown MoSe₂ on hBN at 500 °C and 250 °C, compared to mechanically exfoliated MoSe₂ on hBN. (c, d) Raman spectra of grown samples at different conditions in comparison to mechanically exfoliated monolayer MoSe₂ on SiO₂/Si. (d) Zoomed-in spectrum showing the weaker secondary peaks, as highlighted.
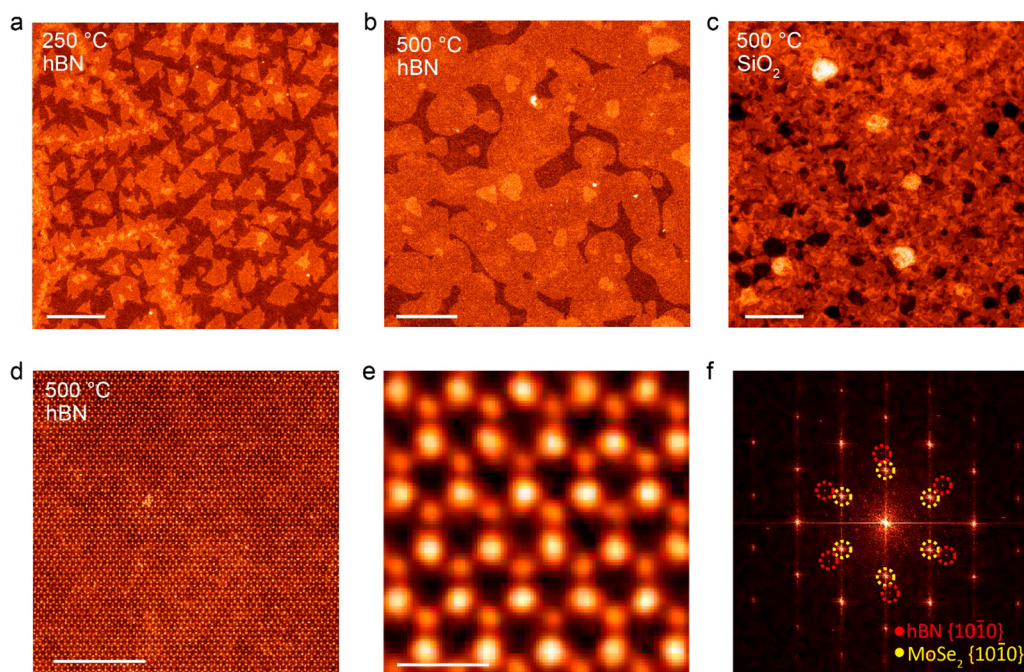
Figure 3. STEM−ADF characterization of MBE-grown MoSe$_2$ on hBN at 250 °C (a) and 500 °C (b), and on SiO$_2$/Si at 500 °C (c), respectively. Atomic resolution STEM−ADF images (d, e) of MBE-grown MoSe$_2$ on hBN at 500 °C and the corresponding (f) FFT image. The MoSe$_2$ FFT spots in (f) are highlighted by yellow dashed circles and the hBN spots by red dashed circles. Scale bar: 200 nm in (a−c), 5 nm in (d), 0.5 nm in (e).

significantly (Figure S2). Therefore, it can be concluded that high substrate temperature (≤500 °C) and high selenium flux is essential to obtain isotropic domains[55] which can facilitate the seamless merging of grains.

For comparison, we also performed MBE growth on a nonepitaxial substrate, SiO$_2$/Si. The same growth condition of 500 °C and Se/Mo flux ratio of ∼20:1 was used. It can be clearly seen (Figure 1g-i) that the grains are much smaller compared to growth on hBN. Varying the growth conditions in terms of flux and temperature did not result in an increase in the grain size.

Detailed spectroscopic characterizations were performed *ex situ* to characterize the MBE-grown samples. X-ray photo-emission spectroscopy (XPS) peaks with binding energies of 232.1, 228.9, 55.5, and 54.6 eV can be assigned to the core level orbitals of Mo 3d$_{3/2}$, Mo 3d$_{5/2}$, Se 3d$_{3/2}$, and Se 3d$_{5/2}$, respectively, in good agreement with previous studies[30] and the bulk single crystal reference sample measured (Figure 2a). Elemental composition analysis indicates that the Mo/Se ratio is 1:2. Importantly, no oxidation peaks of Mo(VI) were observed despite exposing the sample to air, which verifies that the samples have a low density of defects.[56] The photo-luminescence (PL) measured from the MoSe$_2$ grown on hBN at 500 °C has intensity and full width half-maximum (fwhm) comparable to that of mechanically exfoliated MoSe$_2$ on hBN, which signifies the high crystallinity of the grown film (Figure 2b). In comparison, the growth at 250 °C on hBN has poor crystallinity and low PL intensity. The Raman peaks at 241.9 and 287.6 cm^{-1} observed in the spectra (Figure 2c,d) are assigned to the signature A$_{1g}$ and E$^2_{2g}$ vibrational modes of MoSe$_2$ respectively. Remarkably, the secondary fingerprint peaks[57,58] of MoSe$_2$ grown on hBN at 500 °C are clearly resolved (highlighted in Figure 2d) and match well with that of exfoliated monolayer MoSe$_2$. On the other hand, the secondary

Raman fingerprint peaks of MoSe$_2$ grown at 250 °C and on SiO$_2$/Si, show broad peaks, signifying a poorer crystallinity for these samples.

To evaluate the crystallinity of MoSe$_2$ grown at different temperatures and on different substrates, we performed scanning transmission electron microscopy−annular dark field (STEM−ADF) imaging. The grains grown on hBN at 250 °C are found to have an average size of ∼75 nm (Figure 3a), which increased to ∼200 nm when grown at 500 °C (Figure 3b). Grains grown on SiO$_2$/Si have the smallest size of <10 nm and exhibit nonuniform thickness even at such small length scale (Figure 3c). The atomic resolution STEM−ADF image of monolayer MoSe$_2$ reveals the long-range periodic bright and dim columns of the MoSe$_2$ honeycomb pattern, which represent the Se$_2$ and Mo atoms respectively (Figure 3d,e). The image contrast of the STEM image is directly proportional to the atomic number Z as about Z$^{1.67}$,[59] this factor renders the underlying hBN lattice invisible in the presence of MoSe$_2$ due to the huge Z atom number variations. The average lattice constant measured from the atomic resolution images for all three samples is 3.29 Å, which is similar to that of bulk MoSe$_2$,[60] indicating that there is negligible strain between the vdW epitaxially grown layer and hBN substrate (lattice constant of 2.50 Å[61]). The fast Fourier transform (FFT) analysis shows that the MoSe$_2$ grains grown at 500 °C on hBN are well-oriented with its diffraction spots aligned with those of the underlying hBN substrate (Figure 3f).

The merging of misoriented grains occurs *via* grain boundary (GB), thus analyzing the distribution and morphol-ogy of GBs for films grown at different temperature provide crucial information about the grain coalescence process. Due to the 6-fold symmetry in MoSe$_2$, the diffraction spots indicate that the grains are either perfectly aligned and merged flawlessly without GBs,[55] or rotated 60° with respect to each
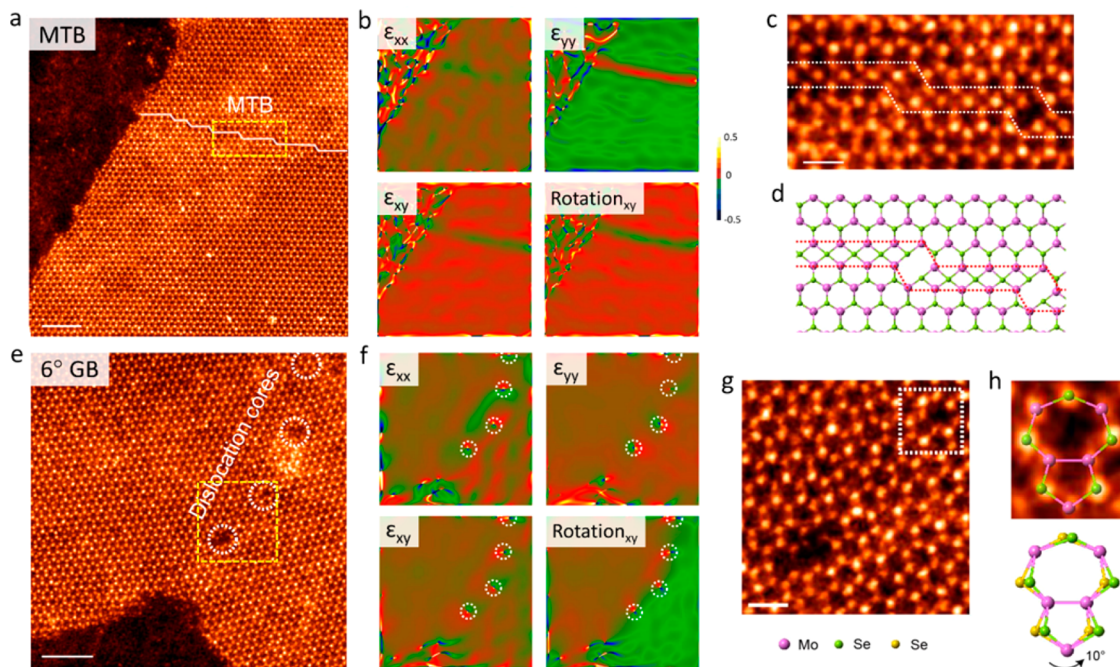
Figure 4. Electron microscope analysis of GBs in MBE-grown monolayer MoSe$_2$ on hBN. (a) Atomic resolution STEM−ADF image of the 500 °C grown MoSe$_2$ film with MTB. (b) Strain analysis of (a) with the matrix series ε_{xx}, ε_{xy}, ε_{yy} and rotation$_{xy}$. (c) Enlarged yellow box region in (a) showing the atomic structure of the MTB as highlighted by the white dashed line and (d) the corresponding atomic model. (e) Atomic resolution STEM−ADF image of the 250 °C grown MoSe$_2$ film with 6° tilt GB. (f) Strain analysis of (e) with the matrix series ε_{xx}, ε_{xy}, ε_{yy}, and rotation$_{xy}$ (g) Enlarged yellow box region in (e) showing the presence of dislocation cores. (h) Enlarged white box region in (g) showing the 5|7-fold ring dislocation core. A schematic of the dislocation cores is overlaid across the STEM image and also depicted on the lower panel. Scale bars: 2 nm (a, e); 0.5 nm (c, g).
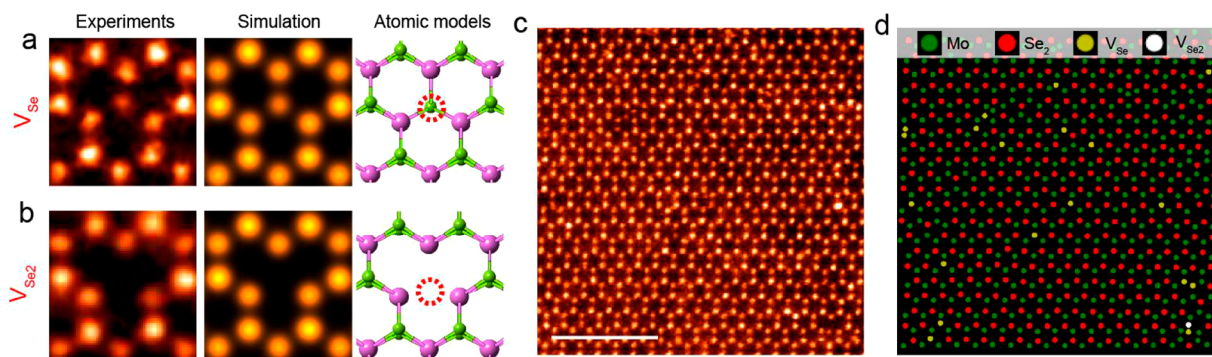

Figure 5. Atomic-level defect analysis in MBE-grown monolayer MoSe$_2$ films. Atomic resolution STEM−ADF images of (a) V_{Se} and (b) V_{Se2} sites, with corresponding simulations and atomic models depicted on the right panels. (c) Atomic-resolution STEM−ADF image of a typical monolayer MoSe$_2$ film grown on hBN at 500 °C. (d) Atomic structure model based on a histogram analysis. The Mo, Se$_2$, V_{Se}, and V_{Se2} sites, respectively, are illustrated by green, red, yellow, and white balls. Scale bar: 2 nm.

other, merging by mirror twin boundaries (MTBs). At growth temperature of 500 °C on hBN, the GBs observed in the MoSe$_2$ film are mainly MTBs (Figure 4a). To evaluate the associated strain or imperfections along the merging regions, geometric phase analysis[62] using the symmetric strain matrix components (ε_{xx}, ε_{xy}, ε_{yy}, and rotation$_{xy}$) was applied. Notably, the strain concentrates along the MTB and does not propagate into the adjacent pristine lattices as verified by various strain matrix series (Figure 4b). No dislocation cores are found along the MTB regions. Although theoretical calculations[63] predict around 10 types of MTBs in group VIB TMDC films, experimentally observed MTBs in MBE grown MoSe$_2$ film are mainly the 4|4P-type,[64] which is characterized by 4-fold rings with Se dimer as sharing sites (Figure 4c). It has been reported

that the 4|4P-type MTB is metallic and shows charge density wave order.[41] The MTB is not perfectly straight and two shifted 4|4P segments are linked by a octahedron kink as shown in Figure 4d. In contrast, growth at 250 °C results in both MTBs and low-angle tilted GBs of less than 10° misorientation. A typical tilted GB with 6° misorientation is depicted in Figure 4e, a few dislocation cores (Figure 4f) were observed along the titled GB as highlighted by the white dashed circles. The dislocation core reveals an irregular 5|7-fold ring (Figure 4g,h). The 5|7-fold dislocation cores were found to impede electrical conductance as they introduce a series of localized midgap states that can serve as sinks for charge carriers.[65,66] In comparison, growth on SiO$_2$/Si produces polycrystalline films with domains of different
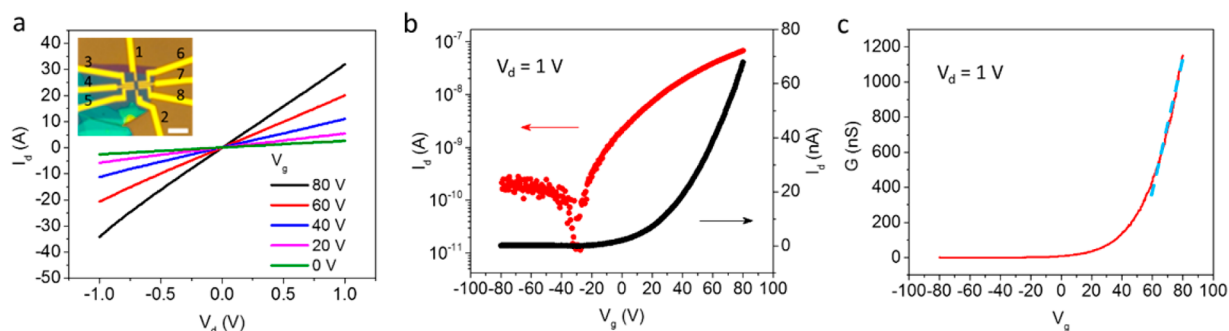
Figure 6. Transport properties of MBE-grown $MoSe_2$ on hBN substrates. (a) Output characteristics of $MoSe_2$ FET at various back gate voltages. Scale bar of inset: 5 um. (b) Two-probe transfer curves of the back-gated device measured at room temperature. (c) Four-probe conductance plot with respect to the back gate voltage. The dashed line shows the linear fit. The data shown here use leads 1 and 2 as source and drain, and for (c) leads 6 and 8 were used to record the voltage.

orientations (0 to 60°), and comprises of mainly tilt GBs (Figure S3).

The presence of point defects in TMDC films, in particular chalcogen vacancies, has a critical effect on the electronic properties of the TMDC films.[67] The density of chalcogen vacancies is a crucial determinant of the film quality. To quantitatively calculate the density of chalcogen vacancies of the optimized MBE-grown $MoSe_2$ films, we employed Python scripts[68] and massively processed the as-captured images. Since the intensity contrast in ADF images is approximately proportional to $Z^{1.67}$, the presence of single Se vacancies (V_{Se}) (Figure 5a) and double Se vacancies (V_{Se2}) (Figure 5b) can be identified by the image contrast variations as confirmed by the combined experimental and simulation results. An example is illustrated in Figure 5c and d. Mo (green blob), Se_2 (red blob), V_{Se} (yellow blob), and V_{Se2} (white blob) sites from the raw image (Figure 5c) can be effectively identified by the Python scripts with high accuracy and efficiency (Figure 5d) based on the image intensity. Importantly, negligible Mo vacancy, antisite or interstitial defects are found. The calculated V_{Se} and V_{Se2} defect densities are $V_{Se} = 0.88$ nm^{-2} and $V_{Se2} = 0.06$ nm^{-2}, which are much lower than in $MoSe_2$ single crystals grown by CVD of ref 34 (Figure S4).

To evaluate the electrical performance of the grown film, FETs were fabricated on the 500 °C grown $MoSe_2$, with the hBN substrate as the dielectric layer. Four-probe measurements (a typical device image is shown in the inset of Figure 6a) were performed using different combinations of leads, to ensure repeatability of results. Electrical measurements were carried out in a nitrogen-filled glovebox at room temperature with a probe station. Figure 6a shows representative output performance of a device measured with lead 1 as source and lead 2 as drain. The linear behavior of $I_d - V_d$ curves at different gate voltages indicates that the contacts at the source and drain electrodes are ohmic. Figure 6b shows the transfer characteristics with a gate bias from −80 to +80 V. As shown, the I_d increases monotonically with increasingly positive V_g, indicating a typical n-type FET behavior, and on/off ratio in the order of 10^4. Using the formula $\mu = (\frac{1}{C_{ox}})(\frac{dG}{dV_g})(\frac{L}{W})$, where μ is field-effect mobility, C_{ox} is the capacitance, G is the measured four-probe conductance, $\frac{dG}{dV_g}$ is extracted from the linear part of the four-probe transfer curve, L and W is length and width of the channel respectively, the average μ is extracted to be ~14.7 ± 0.8 cm^2 V^{-1} s^{-1}. The extracted mobility is more than 2 orders of magnitude higher than previously reported MBE-

grown $MoSe_2$ on GaAs(111) and is comparable to CVD-grown samples with values ranging from 0.02 to 95 $cm^2/(V s)$ (Table I). It is noted that most of the previously reported MBE growth studies rarely report on charge transport properties.[19,37,40−46]

CONCLUSION

In conclusion, we have successfully demonstrated the growth of high quality 1−2 layers $MoSe_2$ films on hBN using MBE. Crystalline $MoSe_2$ films can be grown at temperature as low as 250 °C on hBN. The highest quality film was grown at a substrate temperature of 500 °C and under a large Se:Mo ratio. STEM analyses of the 500 °C grown film show that they are mostly coalesced from grains that are highly oriented, giving rise to boundary-free regions; in some regions MTBs exist to merge 60° misoriented grains. XPS and Raman spectroscopy verified that the MBE-grown film has comparable quality to that of single crystal. Transport results indicate a relatively high electron mobility of ~14.7 ± 0.8 $cm^2/(V s)$, which can be attributed to the high crystallinity of the film grown by van der Waals epitaxy on hBN substrate.

METHODS

The growth is demonstrated on mechanical exfoliated hBN on 285 nm SiO_2/Si substrate, as prepared via the typical adhesive tape technique.[69] $MoSe_2$ film was grown using a MBE chamber with a base pressure ~6 × 10^{-10} Torr. Prior to growth, the substrate was degassed in an ultrahigh vacuum chamber for 1 h and annealed at 600 °C for 5 min. Ultrapure Mo rod (99.99%) and Se pellets (99.999%) were evaporated from an electron beam evaporator and a standard Knudsen cell, respectively. For all the experiments, the temperature of Se crucible cell was maintained at 180 °C with the cracker at 220 °C. The flux ratio of Se/Mo was ~20:1. The chamber pressure during growth was ~1 × 10^{-8} Torr.

Atomic force microscopy was performed using a Bruker Dimension FastScan atomic force microscope in tapping mode at room temperature. Raman spectra were recorded at room temperature using the confocal WiTec Alpha 300R Raman microscope with laser excitation at 532 nm and power of <300 μW. Scanning transmission electron microscopy−annular dark field (STEM−ADF) was performed using an aberration-corrected Nion UltraSTEM-100, equipped with a cold field emission gun, operating at 100 kV. XPS measurements were carried out using SPECS XR-50 X-ray Mg Ka source with the pass energy of 30 eV and spot size of 5 mm, in chamber pressure <8 × 10^{-10} mbar. XPS peak fitting was carried out using a mixed Gaussian−Lorentzian function after a Shirley background subtraction. FET devices were fabricated using standard electron-beam lithography procedures to pattern the samples with metal electrodes, in which Cr/Au of 2 nm/50 nm were deposited

through thermal evaporation. All the electrical transport measurements were performed in a glovebox filled with nitrogen gas.

ASSOCIATED CONTENT

Ⓢ Supporting Information

The Supporting Information is available free of charge on the ACS Publications website at DOI: 10.1021/acsnano.8b04037.

(PDF)

AUTHOR INFORMATION

Corresponding Author

*E-mail: chmlohkp@nus.edu.sg.

ORCID Ⓞ

Sock Mui Poh: 0000-0002-6289-4519

Xiaoxu Zhao: 0000-0001-9746-3770

Sherman Jun Rong Tan: 0000-0003-1591-3497

Deyi Fu: 0000-0003-1365-8963

Kian Ping Loh: 0000-0002-1491-743X

Author Contributions

&S.M.P. amd X.Z. contributed equally.

Notes

The authors declare no competing financial interest.

REFERENCES

(1) Mak, K. F.; Lee, C.; Hone, J.; Shan, J.; Heinz, T. F. Atomically Thin MoS2: A New Direct-Gap Semiconductor. *Phys. Rev. Lett.* **2010**, *105*, 136805.

(2) Xiao, D.; Liu, G.-B.; Feng, W.; Xu, X.; Yao, W. Coupled Spin and Valley Physics in Monolayers of MoS2 and Other Group-VI Dichalcogenides. *Phys. Rev. Lett.* **2012**, *108*, 196802.

(3) Klanjšek, M.; Zorko, A.; Žitko, R.; Mravlje, J.; Jagličić, Z.; Biswas, P. K.; Prelovšek, P.; Mihailovic, D.; Arčon, D. A High-Temperature Quantum Spin Liquid with Polaron Spins. *Nat. Phys.* **2017**, *13*, 1130.

(4) Xi, X.; Zhao, L.; Wang, Z.; Berger, H.; Forró, L.; Shan, J.; Mak, K. F. Strongly Enhanced Charge-Density-Wave Order in Monolayer NbSe2. *Nat. Nanotechnol.* **2015**, *10*, 765.

(5) Soluyanov, A. A.; Gresch, D.; Wang, Z.; Wu, Q.; Troyer, M.; Dai, X.; Bernevig, B. A. Type-II Weyl Semimetals. *Nature* **2015**, *527*, 495.

(6) Kiss, T.; Yokoya, T.; Chainani, A.; Shin, S.; Hanaguri, T.; Nohara, M.; Takagi, H. Charge-Order-Maximized Momentum-Dependent Superconductivity. *Nat. Phys.* **2007**, *3*, 720.

(7) Radisavljevic, B.; Radenovic, A.; Brivio, J.; Giacometti, V.; Kis, A. Single-Layer MoS2 Transistors. *Nat. Nanotechnol.* **2011**, *6*, 147.

(8) Sangwan, V. K.; Jariwala, D.; Kim, I. S.; Chen, K.-S.; Marks, T. J.; Lauhon, L. J.; Hersam, M. C. Gate-Tunable Memristive Phenomena Mediated By Grain Boundaries in Single-Layer MoS2. *Nat. Nanotechnol.* **2015**, *10*, 403.

(9) Wang, Y.; Liu, E.; Liu, H.; Pan, Y.; Zhang, L.; Zeng, J.; Fu, Y.; Wang, M.; Xu, K.; Huang, Z.; Wang, Z.; Lu, H.-Z.; Xing, D.; Wang, B.; Wan, X.; Miao, F. Gate-Tunable Negative Longitudinal Magnetoresistance in the Predicted Type-II Weyl Semimetal WTe2. *Nat. Commun.* **2016**, *7*, 13142.

(10) Ye, J. T.; Zhang, Y. J.; Akashi, R.; Bahramy, M. S.; Arita, R.; Iwasa, Y. Superconducting Dome in a Gate-Tuned Band Insulator. *Science* **2012**, *338*, 1193.

(11) Yin, Z.; Li, H.; Li, H.; Jiang, L.; Shi, Y.; Sun, Y.; Lu, G.; Zhang, Q.; Chen, X.; Zhang, H. Single-Layer MoS2 Phototransistors. *ACS Nano* **2012**, *6*, 74−80.

(12) Lopez-Sanchez, O.; Lembke, D.; Kayci, M.; Radenovic, A.; Kis, A. Ultrasensitive Photodetectors Based on Monolayer MoS2. *Nat. Nanotechnol.* **2013**, *8*, 497.

(13) Yuan, H.; Wang, X.; Lian, B.; Zhang, H.; Fang, X.; Shen, B.; Xu, G.; Xu, Y.; Zhang, S.-C.; Hwang, H. Y.; Cui, Y. Generation and Electric Control of Spin−Valley-Coupled Circular Photogalvanic Current in WSe2. *Nat. Nanotechnol.* **2014**, *9*, 851.

(14) Zhang, X.-X.; Cao, T.; Lu, Z.; Lin, Y.-C.; Zhang, F.; Wang, Y.; Li, Z.; Hone, J. C.; Robinson, J. A.; Smirnov, D.; Louie, S. G.; Heinz, T. F. Magnetic Brightening and Control of Dark Excitons in Monolayer WSe2. *Nat. Nanotechnol.* **2017**, *12*, 883.

(15) Liu, C.; Kong, D.; Hsu, P.-C.; Yuan, H.; Lee, H.-W.; Liu, Y.; Wang, H.; Wang, S.; Yan, K.; Lin, D.; Maraccini, P. A.; Parker, K. M.; Boehm, A. B.; Cui, Y. Rapid Water Disinfection Using Vertically Aligned MoS2 Nanofilms and Visible Light. *Nat. Nanotechnol.* **2016**, *11*, 1098.

(16) Lu, Q.; Yu, Y.; Ma, Q.; Chen, B.; Zhang, H. 2D Transition-Metal-Dichalcogenide-Nanosheet-Based Composites for Photocatalytic and Electrocatalytic Hydrogen Evolution Reactions. *Adv. Mater.* **2016**, *28*, 1917−1933.

(17) Asadi, M.; Kim, K.; Liu, C.; Addepalli, A. V.; Abbasi, P.; Yasaei, P.; Phillips, P.; Behranginia, A.; Cerrato, J. M.; Haasch, R.; Zapol, P.; Kumar, B.; Klie, R. F.; Abiade, J.; Curtiss, L. A.; Salehi-Khojin, A. Nanostructured Transition Metal Dichalcogenide Electrocatalysts for CO2 Reduction in Ionic Liquid. *Science* **2016**, *353*, 467.

(18) Novoselov, K. S.; Jiang, D.; Schedin, F.; Booth, T. J.; Khotkevich, V. V.; Morozov, S. V.; Geim, A. K. Two-dimensional Atomic Crystals. *Proc. Natl. Acad. Sci. U. S. A.* **2005**, *102*, 10451−10453.

(19) Zhang, Y.; Chang, T.-R.; Zhou, B.; Cui, Y.-T.; Yan, H.; Liu, Z.; Schmitt, F.; Lee, J.; Moore, R.; Chen, Y.; Lin, H.; Jeng, H.-T.; Mo, S.-K.; Hussain, Z.; Bansil, A.; Shen, Z.-X. Direct Observation of the Transition from Indirect to Direct Bandgap in Atomically Thin Epitaxial MoSe2. *Nat. Nanotechnol.* **2013**, *9*, 111.

(20) Tonndorf, P.; Schmidt, R.; Böttger, P.; Zhang, X.; Börner, J.; Liebig, A.; Albrecht, M.; Kloc, C.; Gordan, O.; Zahn, D. R. T.; Michaelis de Vasconcellos, S.; Bratschitsch, R. Photoluminescence Emission and Raman Response of Monolayer MoS2, MoSe2, and WSe2. *Opt. Express* **2013**, *21*, 4908−4916.

(21) Kong, D.; Wang, H.; Cha, J. J.; Pasta, M.; Koski, K. J.; Yao, J.; Cui, Y. Synthesis of MoS2 and MoSe2 Films with Vertically Aligned Layers. *Nano Lett.* **2013**, *13*, 1341−1347.

(22) Ross, J. S.; Wu, S.; Yu, H.; Ghimire, N. J.; Jones, A. M.; Aivazian, G.; Yan, J.; Mandrus, D. G.; Xiao, D.; Yao, W.; Xu, X. Electrical Control of Neutral and Charged Excitons in a Monolayer Semiconductor. *Nat. Commun.* **2013**, *4*, 1474.

(23) Tongay, S.; Zhou, J.; Ataca, C.; Lo, K.; Matthews, T. S.; Li, J.; Grossman, J. C.; Wu, J. Thermally Driven Crossover from Indirect toward Direct Bandgap in 2D Semiconductors: MoSe2 *versus* MoS2. *Nano Lett.* **2012**, *12*, 5576−5580.

(24) Bernardi, M.; Palummo, M.; Grossman, J. C. Extraordinary Sunlight Absorption and One Nanometer Thick Photovoltaics Using Two-Dimensional Monolayer Materials. *Nano Lett.* **2013**, *13*, 3664−3670.

(25) Chang, Y.-H.; Zhang, W.; Zhu, Y.; Han, Y.; Pu, J.; Chang, J.-K.; Hsu, W.-T.; Huang, J.-K.; Hsu, C.-L.; Chiu, M.-H.; Takenobu, T.; Li, H.; Wu, C.-I.; Chang, W.-H.; Wee, A. T. S.; Li, L.-J. Monolayer MoSe2 Grown by Chemical Vapor Deposition for Fast Photodetection. *ACS Nano* **2014**, *8*, 8582−8590.

(26) Kang, K.; Xie, S.; Huang, L.; Han, Y.; Huang, P. Y.; Mak, K. F.; Kim, C.-J.; Muller, D.; Park, J. High-Mobility Three-Atom-Thick Semiconducting Films with Wafer-Scale Homogeneity. *Nature* **2015**, *520*, 656.

(27) Lu, X.; Utama, M. I. B.; Lin, J.; Gong, X.; Zhang, J.; Zhao, Y.; Pantelides, S. T.; Wang, J.; Dong, Z.; Liu, Z.; Zhou, W.; Xiong, Q.

Large-Area Synthesis of Monolayer and Few-Layer MoSe2 Films on SiO2 Substrates. *Nano Lett.* **2014**, *14*, 2419−2425.

(28) Shaw, J. C.; Zhou, H.; Chen, Y.; Weiss, N. O.; Liu, Y.; Huang, Y.; Duan, X. Chemical Vapor Deposition Growth of Monolayer Mose2 Nanosheets. *Nano Res.* **2014**, *7*, 511−517.

(29) Shim, G. W.; Yoo, K.; Seo, S.-B.; Shin, J.; Jung, D. Y.; Kang, I.-S.; Ahn, C. W.; Cho, B. J.; Choi, S.-Y. Large-Area Single-Layer MoSe2 and Its van der Waals Heterostructures. *ACS Nano* **2014**, *8*, 6655−6662.

(30) Wang, X.; Gong, Y.; Shi, G.; Chow, W. L.; Keyshar, K.; Ye, G.; Vajtai, R.; Lou, J.; Liu, Z.; Ringe, E.; Tay, B. K.; Ajayan, P. M. Chemical Vapor Deposition Growth of Crystalline Monolayer MoSe2. *ACS Nano* **2014**, *8*, 5125−5131.

(31) Xia, J.; Huang, X.; Liu, L.-Z.; Wang, M.; Wang, L.; Huang, B.; Zhu, D.-D.; Li, J.-J.; Gu, C.-Z.; Meng, X.-M. CVD Synthesis of Large-Area, Highly Crystalline Mose2 Atomic Layers on Diverse Substrates and Application to Photodetectors. *Nanoscale* **2014**, *6*, 8949−8955.

(32) Jung, C.; Kim, S. M.; Moon, H.; Han, G.; Kwon, J.; Hong, Y. K.; Omkaram, I.; Yoon, Y.; Kim, S.; Park, J. Highly Crystalline CVD-grown Multilayer MoSe2 Thin Film Transistor for Fast Photodetector. *Sci. Rep.* **2015**, *5*, 15313.

(33) Gong, Y.; Ye, G.; Lei, S.; Shi, G.; He, Y.; Lin, J.; Zhang, X.; Vajtai, R.; Pantelides, S. T.; Zhou, W.; Li, B.; Ajayan, P. M. Synthesis of Millimeter-Scale Transition Metal Dichalcogenides Single Crystals. *Adv. Funct. Mater.* **2016**, *26*, 2009−2015.

(34) Chen, J.; Zhao, X.; Tan, S. J. R.; Xu, H.; Wu, B.; Liu, B.; Fu, D.; Fu, W.; Geng, D.; Liu, Y.; Liu, W.; Tang, W.; Li, L.; Zhou, W.; Sum, T. C.; Loh, K. P. Chemical Vapor Deposition of Large-Size Monolayer MoSe2 Crystals on Molten Glass. *J. Am. Chem. Soc.* **2017**, *139*, 1073−1076.

(35) Chamlagain, B.; Li, Q.; Ghimire, N. J.; Chuang, H.-J.; Perera, M. M.; Tu, H.; Xu, Y.; Pan, M.; Xaio, D.; Yan, J.; Mandrus, D.; Zhou, Z. Mobility Improvement and Temperature Dependence in MoSe2 Field-Effect Transistors on Parylene-C Substrate. *ACS Nano* **2014**, *8*, 5079−5088.

(36) Rhyee, J.-S.; Kwon, J.; Dak, P.; Kim, J. H.; Kim, S. M.; Park, J.; Hong, Y. K.; Song, W. G.; Omkaram, I.; Alam, M. A.; Kim, S. High-Mobility Transistors Based on Large-Area and Highly Crystalline CVD-Grown MoSe2 Films on Insulating Substrates. *Adv. Mater.* **2016**, *28*, 2316−2321.

(37) Xenogiannopoulou, E.; Tsipas, P.; Aretouli, K. E.; Tsoutsou, D.; Giamini, S. A.; Bazioti, C.; Dimitrakopulos, G. P.; Komninou, P.; Brems, S.; Huyghebaert, C.; Radu, I. P.; Dimoulas, A. High-Quality, Large-Area Mose2 and MoSe2/Bi2Se3 Heterostructures on AlN(0001)/Si(111) substrates by Molecular Beam Epitaxy. *Nanoscale* **2015**, *7*, 7896−7905.

(38) Dau, M. T.; Vergnaud, C.; Marty, A.; Rortais, F.; Beigné, C.; Boukari, H.; Bellet-Amalric, E.; Guigoz, V.; Renault, O.; Alvarez, C.; Okuno, H.; Pochet, P.; Jamet, M. Millimeter-Scale Layered Mose2 Grown on Sapphire and Evidence for Negative Magnetoresistance. *Appl. Phys. Lett.* **2017**, *110*, 011909.

(39) Roy, A.; Movva, H. C. P.; Satpati, B.; Kim, K.; Dey, R.; Rai, A.; Pramanik, T.; Guchhait, S.; Tutuc, E.; Banerjee, S. K. Structural and Electrical Properties of MoTe2 and MoSe2 Grown by Molecular Beam Epitaxy. *ACS Appl. Mater. Interfaces* **2016**, *8*, 7396−7402.

(40) Ugeda, M. M.; Bradley, A. J.; Shi, S.-F.; da Jornada, F. H.; Zhang, Y.; Qiu, D. Y.; Ruan, W.; Mo, S.-K.; Hussain, Z.; Shen, Z.-X.; Wang, F.; Louie, S. G.; Crommie, M. F. Giant Bandgap Renormalization and Excitonic Effects in a Monolayer Transition Metal Dichalcogenide Semiconductor. *Nat. Mater.* **2014**, *13*, 1091.

(41) Barja, S.; Wickenburg, S.; Liu, Z.-F.; Zhang, Y.; Ryu, H.; Ugeda, M. M.; Hussain, Z.; Shen, Z.-X.; Mo, S.-K.; Wong, E.; Salmeron, Miquel B.; Wang, F.; Crommie, M. F.; Ogletree, D. F.; Neaton, Jeffrey B.; Weber-Bargioni, A. Charge Density Wave Order in 1D Mirror Twin Boundaries of Single-Layer MoSe2. *Nat. Phys.* **2016**, *12*, 751.

(42) Jiao, L.; Liu, H. J.; Chen, J. L.; Yi, Y.; Chen, W. G.; Cai, Y.; Wang, J. N.; Dai, X. Q.; Wang, N.; Ho, W. K.; Xie, M. H. Molecular-Beam Epitaxy of Monolayer MoSe2: growth Characteristics and Domain Boundary Formation. *New J. Phys.* **2015**, *17*, 053023.

(43) Choi, B. K.; Kim, M.; Jung, K.-H.; Kim, J.; Yu, K.-S.; Chang, Y. J. Temperature Dependence of Band Gap in MoSe2 Grown by Molecular Beam Epitaxy. *Nanoscale Res. Lett.* **2017**, *12*, 492.

(44) Ma, Y.; Kolekar, S.; Coy Diaz, H.; Aprojanz, J.; Miccoli, I.; Tegenkamp, C.; Batzill, M. Metallic Twin Grain Boundaries Embedded in MoSe2Monolayers Grown by Molecular Beam Epitaxy. *ACS Nano* **2017**, *11*, 5130−5139.

(45) Vishwanath, S.; Liu, X.; Rouvimov, S.; Mende, P. C.; Azcatl, A.; McDonnell, S.; Wallace, R. M.; Feenstra, R. M.; Furdyna, J. K.; Jena, D.; King, H. G. Comprehensive structural and Optical Characterization of MBE Grown Mose2 on Graphite, CaF2 and Graphene. *2D Mater.* **2015**, *2*, 024007.

(46) Choi, Y.-H.; Lim, D.-H.; Jeong, J.-H.; Park, D.; Jeong, K.-S.; Kim, M.; Song, A.; Chung, H.-S.; Chung, K.-B.; Yi, Y.; Cho, M.-H. Characterization of Rotational Stacking Layers in Large-Area MoSe2 Film Grown by Molecular Beam Epitaxy and Interaction with Photon. *ACS Appl. Mater. Interfaces* **2017**, *9*, 30786−30796.

(47) Chen, M.-W.; Ovchinnikov, D.; Lazar, S.; Pizzochero, M.; Whitwick, M. B.; Surrente, A.; Baranowski, M.; Sanchez, O. L.; Gillet, P.; Plochocka, P.; Yazyev, O. V.; Kis, A. Highly Oriented Atomically Thin Ambipolar MoSe2 Grown by Molecular Beam Epitaxy. *ACS Nano* **2017**, *11*, 6355−6361.

(48) Dean, C. R.; Young, A. F.; Meric, I.; Lee, C.; Wang, L.; Sorgenfrei, S.; Watanabe, K.; Taniguchi, T.; Kim, P.; Shepard, K. L.; Hone, J. Boron Nitride Substrates for High-Quality Graphene Electronics. *Nat. Nanotechnol.* **2010**, *5*, 722.

(49) Venables, J. A.; Spiller, G. D. T.; Hanbucken, M. Nucleation and Growth of Thin Films. *Rep. Prog. Phys.* **1984**, *47*, 399.

(50) Zhang, Z.; Lagally, M. G. Atomistic Processes in the Early Stages of Thin-Film Growth. *Science* **1997**, *276*, 377.

(51) Zhou, W.; Zou, X.; Najmaei, S.; Liu, Z.; Shi, Y.; Kong, J.; Lou, J.; Ajayan, P. M.; Yakobson, B. I.; Idrobo, J.-C. Intrinsic Structural Defects in Monolayer Molybdenum Disulfide. *Nano Lett.* **2013**, *13*, 2615−2622.

(52) Poh, S. M.; Tan, S. J. R.; Zhao, X.; Chen, Z.; Abdelwahab, I.; Fu, D.; Xu, H.; Bao, Y.; Zhou, W.; Loh, K. P. Large Area Synthesis of 1D-MoSe2 Using Molecular Beam Epitaxy. *Adv. Mater.* **2017**, *29*, 1605641.

(53) Witten, T. A.; Sander, L. M. Diffusion-Limited Aggregation. *Phys. Rev. B: Condens. Matter Mater. Phys.* **1983**, *27*, 5686−5697.

(54) Yue, R.; Nie, Y.; Walsh, L. A.; Addou, R.; Liang, C.; Lu, N.; Barton, A. T.; Zhu, H.; Che, Z.; Barrera, D.; Cheng, L.; Cha, P.-R.; Chabal, Y. J.; Hsu, J. W. P.; Kim, J.; Kim, M. J.; Colombo, L.; Wallace, R. Mo.; Cho, K.; Hinkle, C. L. Nucleation and Growth of WSe2: Enabling Large Grain Transition Metal Dichalcogenides. *2D Mater.* **2017**, *4*, 045019.

(55) Fu, D.; Zhao, X.; Zhang, Y.-Y.; Li, L.; Xu, H.; Jang, A. R.; Yoon, S. I.; Song, P.; Poh, S. M.; Ren, T.; Ding, Z.; Fu, W.; Shin, T. J.; Shin, H. S.; Pantelides, S. T.; Zhou, W.; Loh, K. P. Molecular Beam Epitaxy of Highly Crystalline Monolayer Molybdenum Disulfide on Hexagonal Boron Nitride. *J. Am. Chem. Soc.* **2017**, *139*, 9392−9400.

(56) Zhu, H.; Qin, X.; Cheng, L.; Azcatl, A.; Kim, J.; Wallace, R. M. Remote Plasma Oxidation and Atomic Layer Etching of MoS2. *ACS Appl. Mater. Interfaces* **2016**, *8*, 19119−26.

(57) Nam, D.; Lee, J.-U.; Cheong, H. Excitation Energy Dependent Raman Spectrum of MoSe2. *Sci. Rep.* **2015**, *5*, 17113.

(58) Zhang, M.; Wu, J.; Zhu, Y.; Dumcenco, D. O.; Hong, J.; Mao, N.; Deng, S.; Chen, Y.; Yang, Y.; Jin, C.; Chaki, S. H.; Huang, Y.-S.; Zhang, J.; Xie, L. Two-Dimensional Molybdenum Tungsten Diselenide Alloys: Photoluminescence, Raman Scattering, and Electrical Transport. *ACS Nano* **2014**, *8*, 7130−7137.

(59) Krivanek, O. L.; Chisholm, M. F.; Nicolosi, V.; Pennycook, T. J.; Corbin, G. J.; Dellby, N.; Murfitt, M. F.; Own, C. S.; Szilagyi, Z. S.; Oxley, M. P.; Pantelides, S. T.; Pennycook, S. J. Atom-By-Atom Structural and Chemical Analysis by Annular Dark-Field Electron Microscopy. *Nature* **2010**, *464*, 571.

(60) Yun, W. S.; Han, S. W.; Hong, S. C.; Kim, I. G.; Lee, J. D. Thickness and Strain Effects on Electronic Structures of Transition Metal Dichalcogenides: 2H-MX2 semiconductors (M = Mo, W; X =

S, Se, Te). *Phys. Rev. B: Condens. Matter Mater. Phys.* **2012**, *85*, 033305.

(61) Ooi, N.; Rajan, V.; Gottlieb, J.; Catherine, Y.; Adams, J. B. Structural Properties of Hexagonal Boron Nitride. *Modell. Simul. Mater. Sci. Eng.* **2006**, *14*, 515.

(62) Hÿtch, M. J.; Snoeck, E.; Kilaas, R. Quantitative Measurement of Displacement and Strain Fields from HREM Micrographs. *Ultramicroscopy* **1998**, *74*, 131−146.

(63) Zou, X.; Yakobson, B. I. Metallic High-Angle Grain Boundaries in Monolayer Polycrystalline WS2. *Small* **2015**, *11*, 4503−4507.

(64) Zhao, X.; Ding, Z.; Chen, J.; Dan, J.; Poh, S. M.; Fu, W.; Pennycook, S. J.; Zhou, W.; Loh, K. P. Strain Modulation by van der Waals Coupling in Bilayer Transition Metal Dichalcogenide. *ACS Nano* **2018**, *12*, 1940−1948.

(65) Azizi, A.; Zou, X.; Ercius, P.; Zhang, Z.; Elías, A. L.; Perea-López, N.; Stone, G.; Terrones, M.; Yakobson, B. I.; Alem, N. Dislocation Motion and Grain Boundary Migration in Two-Dimensional Tungsten Disulphide. *Nat. Commun.* **2014**, *5*, 4867.

(66) Najmaei, S.; Amani, M.; Chin, M. L.; Liu, Z.; Birdwell, A. G.; O'Regan, T. P.; Ajayan, P. M.; Dubey, M.; Lou, J. Electrical Transport Properties of Polycrystalline Monolayer Molybdenum Disulfide. *ACS Nano* **2014**, *8*, 7930−7937.

(67) Komsa, H.-P.; Krasheninnikov, A. V. Native Defects in Bulk and Monolayer MoS2 from First Principles. *Phys. Rev. B: Condens. Matter Mater. Phys.* **2015**, *91*, 125304.

(68) Zhao, X.; Fu, D.; Ding, Z.; Zhang, Y.-Y.; Wan, D.; Tan, S. J. R.; Chen, Z.; Leng, K.; Dan, J.; Fu, W.; Geng, D.; Song, P.; Du, Y.; Venkatesan, T.; Pantelides, S. T.; Pennycook, S. J.; Zhou, W.; Loh, K. P. Mo-Terminated Edge Reconstructions in Nanoporous Molybdenum Disulfide Film. *Nano Lett.* **2018**, *18*, 482−490.

(69) Novoselov, K. S.; Geim, A. K.; Morozov, S. V.; Jiang, D.; Zhang, Y.; Dubonos, S. V.; Grigorieva, I. V.; Firsov, A. A. Electric Field Effect in Atomically Thin Carbon Films. *Science* **2004**, *306*, 666.